Exploring the mechanical properties of additively manufactured carbon-rich zirconia 3D microarchitectures

J.P. Winczewski [a,1,*], S. Zeiler [b,c,1,*], S. Gabel [b], A. Susarrey-Arce [a,*], J.G.E. Gardeniers [a], B. Merle [b,d,*]

[a] Mesoscale Chemical Systems, MESA+ Institute, University of Twente, P.O. Box 217, Enschede 7500 AE, The Netherlands
[b] Materials Science & Engineering, Institute I, Friedrich-Alexander-Universität Erlangen-Nürnberg, Martensstr. 5, 91058 Erlangen, Germany
[c] Department of Materials Science, Montanuniversität Leoben, Roseggerstr. 12, 8700 Leoben, Austria
[d] Institute of Materials Engineering, University of Kassel, Moenchebergstr. 3, 34125 Kassel, Germany

HIGHLIGHTS

- For the first time, carbon's influence on mechanical properties is studied in ceramic microarchitectures fabricated via two-photon lithography.
- Carbon-rich binder remnants can significantly improve the compression strength and ductility of ZrO_2 microarchitectures.
- The likeliest explanation for mechanical behavior is the dual organic-ceramic character, reminiscent of "brick and mortar".
- The t-ZrO_2 micropillars with carbon remnants exhibit strikingly high ductility and strength (3.73 ± 0.21 GPa).
- The carbon-free m-ZrO_2 and t-ZrO_2 micropillars evidence brittle-like failure, at 2.43 ± 0.19 GPa and 1.29 ± 0.33 GPa.

GRAPHICAL ABSTRACT
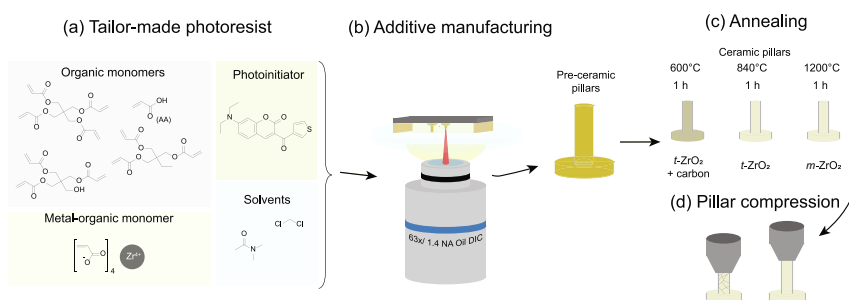
ARTICLE INFO

ABSTRACT

Two-photon lithography (TPL) is a promising technique for manufacturing ceramic microstructures with nanoscale resolution. The process relies on tailor-made precursor resins rich in metal–organic and organic constituents, which can lead to carbon-based residues incorporated within the ceramic microstructures. While these are generally considered unwanted impurities, our study reveals that the presence of carbon-rich residues in the form of graphitic and disordered carbon in tetragonal (t-) ZrO_2 can benefit the mechanical strength of TPL microstructures. In order to achieve a better understanding of these effects, we deconvolute the structural and materials contributions to the strength of the 3D microarchitectures by comparing them to plain micropillars. We vary the organic content by different thermal treatments, resulting in different crystal structures. The highest compression strength of

Micromechanics
Micropillar compression

3.73 ± 0.21 GPa and ductility are reached for the *t*-ZrO$_2$ micropillars, which also contain the highest carbon content. This paradoxical finding opens up new perspectives and will foster the development of "brick and mortar"-like ceramic microarchitectures.

1. Introduction

The growing demand for miniaturization and increased material complexity have long been the impulse to develop various additive manufacturing (AM) methodologies. Several AM techniques, i.e., direct ink writing [1], direct laser writing [2], fused deposition modelling [3], ink-jet printing [4], selective laser sintering [5], stereolithography [6], and two-photon lithography (TPL) [7] have revolutionized the production of three-dimensional (3D) architectures unfeasible using standard fabrication methodologies. Amid the AM techniques, TPL exclusively permits AM of complex 3D microstructures with sub-100 nm resolution [8]. In TPL, a femtosecond laser is typically focused into negative-tone photoresists to initiate two-photon polymerization by radicals or cations locally photogenerated in the focal spot [9,10]. By scanning through the photoresin, photopolymerization is induced in the selected areas, enabling the shaping of material into desired arbitrary microarchitectures [9]. Formerly, microarchitectures realized using TPL demonstrated remarkable electric [11,12], optical [7], piezoelectric [13], superparamagnetic [14] and mechanical [15] properties. The mechanical stability of microstructures fabricated using TPL and strategies for improving their Young's modulus, e.g., through material engineering or varying processing conditions, have been investigated previously [16–21].

Concerning the chemical composition of such microarchitectures, one can especially distinguish organic polymers [22], metal–organic polymers [23], polymers with organic or inorganic fillers [15,24,25], glassy carbon [26], metals [16], or ceramics [17,25]. Alternatively, the surface of polymeric structures can be functionalized, *e.g.*, *via* atomic layer deposition (ALD) [27,28], acting as sacrificial templates to obtain hollow structures, which are subsequently removed by etching [27] or maintained at the surface to access conformal deposition and electrical conductivity in 3D [28]. In the AM of solid-beam metallic and ceramic 3D architectures, dedicated, often tailor-made, photoresins are typically required to attain the target composition. The examples of ceramic materials that have previously been printed *via* TPL include SiOC [29], ZnO [17], TiO$_2$ [30], SnO$_2$ [31], SiO$_2$ [32], and ZrO$_2$ [25,33]. As the metal–organic monomers or organic components often constitute a significant quantity of the photoresins used for manufacturing ceramic microstructures, carbon-based residues might be formed even when annealing in the air. For instance, traces of carbon have been observed in ZnO [17] or TiO$_2$ [30] using Scanning Electron Microscopy – Energy Dispersive Spectroscopy (SEM-EDX). However, the quantitative determination of carbon content based on SEM-EDX analysis is typically inaccurate due to the contamination with hydrocarbons during scanning and the limited sensitivity of the technique toward light elements [30,34].

The presence of carbon in ceramic materials derived from polymers and 3D-printed architectures has been broadly reported and strongly depends on the precursors used and the annealing conditions [17,35]. In our previous study, using cathodoluminescence, we observed defects related to interstitial carbon (C$_i$) in ZrO$_2$ 3D microstructures obtained using tailor-made photoresists and TPL [33]. Additionally, Raman spectroscopy has been employed to characterize 3D microstructured metal oxides *via* TPL. The focus has usually been on determining the crystallographic phase, typically restricted below 1000 cm^{-1} [25,33,36]. Within that range,

vibrational modes of carbon-based residues are weak or non-existent [37–39]. Interestingly, for the structures printed using SZ2080 resin thermally treated in the air, Padolskytė *et al.* did not record carbon-related vibrational modes in the 1500 – 3500 cm^{-1} range [40]. Still, in a different work, a weak signal at 1606 cm^{-1} was observed after the annealing at 1400 °C [41], likely related to residual graphitic carbon [42]. According to the thermogravimetric analysis (TGA), the thermal decomposition of typically-applied monomers in two-photon lithography, i.e., pentaerythritol tetraacrylate, should be nearly complete above approximately 500 °C [43]. It is reasonable to expect that carbon residues might occasionally be buried within the core of the bulk features of ceramic microstructures if the ceramic materials, e.g., ZnO and ZrO$_2$, are known to crystallize at similar temperatures [17,25,35,44]. This may be pronounced if the nucleation of the ceramic grains proceeds from the outer shell, in turn modifying the porosity of the structure and influencing the mass and heat transfer towards the center of the beams.

ZrO$_2$ is recognized for valuable optical, electronic, physicochemical, and mechanical properties [45,46]. Given these desirable characteristics, it has been broadly applied, e.g., in catalysis [47], optics [48], or dentistry [49]. To permit the advanced applications of ZrO$_2$, it is essential to control the crystallographic phase and nanoparticle size distribution alongside permitting the specific structuring of the target architectures. Three polymorphs of zirconia are reported: monoclinic (*m*-ZrO$_2$), tetragonal (*t*-ZrO$_2$), and cubic (*c*-ZrO$_2$) phases, which exist under atmospheric pressure at < 1100 °C, 1100 °C − 2370 °C, and > 2370 °C respectively [50]. The polymorphs may additionally exhibit metastable, stabilized, or strained states [51,52]. The occurrence of a ZrO$_2$ phase strongly depends on the synthesis approach, thermal processing conditions, particle morphology, and defects [45]. Various Zr-containing photoresins suitable for TPL have been investigated to date. Initial studies explored only the optical properties and applications of the printed 3D metal–organic polymeric architectures, and the Zr-doped microstructures remained unannealed [53,54]. The approach of Ovsianikov *et al.* has been adopted in follow-up studies to obtain ceramic structures after thermal treatment, which consisted of a mixed SiO$_2$ (cristoballite) and *t*-ZrO$_2$ [41]. The seminal work of Desponds *et al.* recently presented the application of acrylate resin containing zirconium bromonorbornanelactone carboxylate, which yielded *t*-ZrO$_2$ and *m*-ZrO$_2$ microstructures upon calcination [25]. The study also demonstrated the application of resins loaded with *c*-ZrO$_2$ nanoparticles functionalized with 2-carboxyethyl acrylate [25]. Interestingly, the microstructures fabricated using the latter resin showed lower mechanical stability than when the organo-metallic resin was applied [25]. The results from the acrylate resin (without *c*-ZrO$_2$ nanoparticles) align with our previous results, where we presented a resin, including zirconium-acylate, which permits the manufacturing of *t*-ZrO$_2$ and *m*-ZrO$_2$ after annealing in the air [33,55].

In the ZrO$_2$ microarchitectures presented in the study of Desponds *et al.* [25], no accurate conclusions on the mechanical properties have been drawn due to a combination of bending, compression, and tensile loads within the microstructures. In comparison, other authors used TPL to manufacture micropillars from pyrolytic carbon and benchmarked the intrinsic mechanical properties as a function of the printing parameters [56]. To our knowl-

edge, no such tests have yet been performed on ZrO_2. Experiments with ZrO_2 on a macroscopic level resulted in measured compression strengths between 1.2 GPa and 5.2 GPa (average 2 GPa) [57,58].

In this study, we uncover that the compression strengths of the fabricated ZrO_2 micropillars can be significantly improved when carbon-rich binder remnants are present in the structure. Micropillar compression tests single out the material strength of the composite, while the structural influence is showcased for two different microarchitectures (Kelvin cell and rhombicuboctahedron-inspired cell). These findings further underline the importance and opportunities of studying the carbon content in TPL ceramic microarchitectures. The results can pave the path for fabricating larger ZrO_2 architectures using conventional printing techniques, e.g., SLA and DPL.

2. Materials and methods

2.1. Materials

Acrylic acid (AA; 99%, stabilized with ≈200 ppm 4-methoxyphenol) and dichloromethane (DCM; HPLC grade, ≥99.7+ %, stabilized with amylene) were purchased from Alfa-Aesar. A pentaerythritol tetraacrylate, pentaerythritol triacrylate, and trimethylolpropane triacrylate mixture (PETTA, PETA, TMPTA), methanol (anhydrous, 99.8%) N,N-dimethylacetamide (DMAc; anhydrous, 99.8%), and zirconium acrylate (ZrA) were purchased from Sigma-Aldrich. J&K Scientific delivered 7-diethylamino-3-thenoylcoumarin (DETC; 97%). Acetone, ethanol, and isopropanol, used for cleaning, all of 100% purity, were obtained from Boom B. V. All reagents were used as received; no additional purification was applied.

2.2. Methods

2.2.1. General considerations

To fabricate ZrO_2-based microstructures, a preceramic photoresin suitable for two-photon lithography is prepared. The photoresin contains monomeric species, including a mixture of multifunctional acrylate monomers (PETTA, PETA, and TMPTA), acting as crosslinking agents, mixed with acrylic acid, acting as a dissolution agent for zirconium acrylate, a metal-rich precursor. The latter is the source of Zr for the formation of ZrO_2 ceramics. Dimethylacetamide is chosen as a solvent due to the previously observed good solubility of inorganic and organometallic additives, such as zirconium acrylate, which provides a stable relative concentration of components during the extended printing times required to prepare multiple microarchitectures [33,59]. Owing to the high solubility in acrylates and the efficient radical generation under 780 nm laser excitation, 7-Diethylamino-3-thenoylcoumarin (DETC) is used as a two-photon photoinitiator [60].

2.2.2. Preparation of the preceramic photoresin

Before the preparation, the glassware was cleaned with *aqua regia*, ultrapure water from the Milli-Q system, acetone, ethanol, and isopropanol, to ensure the absence of potential organic and inorganic impurities. The photoresins were handled in amber glassware under amber lighting. The methodology described in our previous work was adapted with minor changes [33]. In the 150 mg of acrylic acid (AA), 500 mg of dimethylacetamide (DMAc), and 2 g of dichloromethane (DCM), 75 mg of zirconium acrylate (ZrA) were dissolved by mixing at 40 °C for 45 min. To the solution, 300 mg of the monomeric mixture containing pentaerythritol tetraacrylate (PETTA), pentaerythritol triacrylate (PETA), and

trimethylolpropane triacrylate monomeric (TMPTA) was added and mixed for 15 additional minutes. Then, 23 mg of 7-diethylamino-3-thenoylcoumarin (DETC) and 250 mg of dichloromethane were added and mixed for another 15 min. The flask was connected to a rotavap with a bath set at 40 °C, and dichloromethane was removed under reduced pressure for 45 min.

2.2.3. Additive manufacturing of ZrO_2 micropillars

A commercial two-photon lithography system (Photonic GT, Nanoscribe) with a 63x / 1.4NA oil-immersion objective of a theoretical 370 μm working distance was used. The freshly-prepared orange-yellow preceramic photoresin was pipetted alongside the edge of the Si dice (9 × 9 mm) and placed on the two double-sided polyimide adhesion tape (120 μm thickness) ribbons applied as spacers on the round glass coverslips (170 μm thickness). The substrates were fixed to a sample holder, and a droplet of immersion oil (Immersol 518F, Carl Zeiss) was administered on the bottom side of the glass coverslips contacting the objective. The array of micropillars is printed on the surface of Si dice using 0.4 μm hatching and stitching distance, 1 mm s^{-1} scanning speed, and 19 mW laser power. The process is schematically presented in Fig. 1.

Shortly after, the micropillars were developed twice for 5 min in methanol. Before the thermal treatment, the dried samples were additionally thermally cured at 65 °C for 60 min in an oven (Model ED 23, Binder), facilitating the evaporation of the volatile components potentially trapped within the preceramic architectures.

2.2.4. Uv-cured preceramic polymeric films

The control powders were prepared from the portion of photoresins unused in the TPL process. The photoresins were transferred into Petri dishes (∅10 cm) to form thin films, which were then crosslinked with a commercial ultraviolet curing lamp of 365 nm with a 4 × 9 W halogen light source for 360 min. The collected cured films were placed into the ceramic crucible for subsequent thermal treatment without additional fine grinding to imitate the bulk material properties.

2.2.5. Thermal annealing

The UV-cured resins and their Si dice substrates were placed in alumina crucible boats. These were then inserted into an air chamber oven (LH 15/12, Nabertherm) and thermally treated following a 0.5 °C min^{-1} heating ramp to 350 °C, at which temperature they were kept for 1 h. This pre-curing step was crucial for maintaining the structural integrity of the micropillars. Furthermore, at this temperature, the thermal decomposition of polymers obtained from the used multifunctional monomers (e.g., TMPTA, PETA/PETTA) and a similar photoresin has been confirmed in previous studies *via* thermogravimetric analyses [33,43,61]. Next, the 1 °-C min^{-1} ramp was continued to the target temperature, which was held for 1 h. Afterward, the oven was left to naturally cool to ambient temperature. The process results in shrinkage of the micropillars and oxidation of the Si surface. Most carbon-based components are combusted during the process, and the Zr is transformed into the corresponding metal oxide. The UV-cured preceramic polymeric films were transformed into white powders, which was in close agreement with the theoretical yield based on the Zr content.

2.3. Characterization

2.3.1. Pillar compression experiments

The compression experiments were performed using a Femtotools NMT03 nanomechanical testing system with an 8 μm flat punch tip. The compression tests were performed under displacement control at 20 and 40 nm/s velocities. The micropillars were
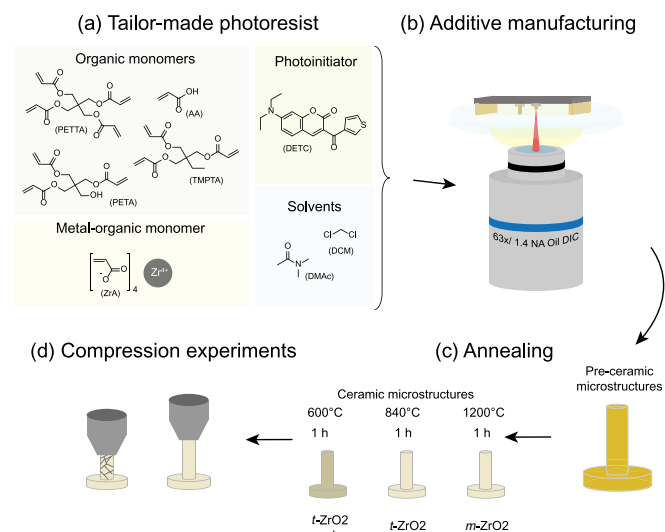
Fig. 1. Schematic presentation of the AM of microstructures: (a) components of the tailor-made photoresist, (b) printing of the microstructures *via* two-photon lithography, (c) annealing in the air, and (d) testing the mechanical stability of miniaturized ceramic pillars *via* compression experiments.

deformed until fracture. The testing system was operated inside a Zeiss Cross Beam 1540 EsB FIB workstation to observe the deformation process *in situ*. A reference test was performed on a plain surface to evaluate the machine stiffness.

2.3.2. Scanning Electron Microscopy (SEM)

The high-resolution images were acquired using a Carl Zeiss Merlin AURIGA CrossBeam workstation at 1.4 kV acceleration voltage. The InLens and High-Efficiency Electron (HE-SE2) detectors were enabled. Additional images were collected using an Ultra High-Resolution Tecan Clara Scanning Electron Microscope at 5–––10 kV acceleration voltage.

2.3.3. Focused ion Beam (FIB)

Cross-sections of the micropillars were milled with Ga ions using an FEI Versa3D Dual Beam and an FEI Helios NanoLab 600i Dual Beam system. Part of the SEM observations was also conducted using this device. The micropillars were partly coated with Pt to avoid curtaining and damage. Some pillars were coated with a thin gold layer to prevent charging effects.

2.3.4. Confocal Raman spectroscopy (Raman)

The room temperature Raman spectra were collected using a Confocal Raman Microscope (Alpha 300, WiTec) in a backscattered configuration with a 600 g/mm grating. The spectra of 3D ceramic structures were collected using a 100x/ 0.9 NA (Olympus, MPLan FL N) objective, and the spectra of the control powders cast on Raman-grade CaF_2 substrates (Knight Optical) were recorded using a 10x/ 0.3 NA (Olympus, MPLan FL N) objective. The samples were excited with a 532 nm laser (frequency-doubled Nd:YAG) at 10 mW, and the data consisted of 10 averaged acquisitions of 25 s, baseline-corrected, and filtered from cosmic rays using CrystalSleuth software [62].

2.3.5. X-ray powder diffraction (XRD)

The control powders were transferred onto zero-diffraction substrates (Bruker) and scanned at a 2θ range of 20 – 80° with 0.02° step size using a benchtop X-ray powder diffractometer (D2 Phaser, Bruker). The instrument had a LynxEye detector and a Cu-Kα source operated at 30 kV and 10 mA. The baseline correction was done using CrystalSleuth software [62].

2.3.6. X-ray photoelectron spectroscopy (XPS)

The X-ray Photoelectron Spectroscopy characterization of the control powders was conducted using a PHI Quantes scanning XPS/HAXPES microprobe, using Al Kα, a monochromatic source at 1486.6 eV (25 W, 15 kV) with a 100 μm spot size. The survey spectra were recorded with 280 eV pass energy with 1 eV step size, and the core spectra were acquired using 112 eV pass energy and 0.1 eV step. The peaks of the synthetic Voigt profile (a convolution of the Lorentzian-Gaussian function) were generated using CasaXPS software. The Tougaard or Shirley profile types were used for the background subtraction. The binding energy was normalized to the fixed aliphatic carbon peak at 284.8 eV. For all the Zr *3d* synthetic peaks, the 2.4 eV binding energy difference (ΔEB) and 0.69 area ratio (Zr $3d_{3/2}$ to Zr $3d_{5/2}$) were used for the deconvolution.

3. Results and discussion

As presented above, the ceramic microstructures were manufactured using a tailor-made photoresin and two-photon lithography combined with subsequent thermal treatment of the printed structures. Here we investigate the chemical composition and the crystallographic phase of the resulting ZrO_2 microarchitectures while their mechanical stability of the microarchitectures properties is tested using *in-situ* compression experiments.

3.1. Chemical characterization of microstructures

Confocal Raman spectroscopy (Raman) provides insight into the crystallographic phases of the ZrO_2 3D micropillars (Fig. 2 (a)). The treatment at 600 °C results in the formation of t-ZrO_2, confirmed by the characteristic B_{1g} and E_g phonon modes [63–65]. The same contributions are observed for the sample annealed at 840 °C. With the increase of the annealing temperature to 840 °C, the half width at half maximum (HWHM) of the E_g mode around 267 cm^{-1} decreases and shifts towards shorter wavenumbers, indicative of the t-ZrO_2 crystallite growth of several nanometers [66]. The sample annealed at 1200 °C presents an m-ZrO_2 phase, confirmed by the presence of the characteristic A_g and B_g phonon modes [64,65,67]. The peak at ∼ 757 cm^{-1} is a second-order *H* group contribution [68].

Next, to investigate the carbon present within the manufactured micropillars, we focus on the 1150 – 1740 cm^{-1} region of Raman spectra, where first-order vibrational modes characteristic of carbon species are present [69]. For all the annealed samples, no vibrational modes at 1635 cm^{-1} (C=C) or 1723 cm^{-1} (C=O) are found, confirming the thermal decomposition of the acrylate resin constituents (Fig. S1(a), Supporting Information) [15]. Considerable carbon-related contributions are observed only for the micropillars annealed at 600 °C, and the spectrum is deconvoluted into four components (Fig. S1(a–b), Supporting Information). The peak at 1359 cm^{-1} is correlated with the defective or disordered carbon lattice (*D*), while the signal at 1596 cm^{-1} is attributed to the graphitic (*G*) carbon species [37,42]. The integrated D and G signals ratio of ∼ 0.69 ($I_D/I_D + I_G$) implies that the carbon residue composition is similar to carbon black or activated carbon [69]. The band peak 1541 cm^{-1} (*D''*) is correlated with the amorphous phase, and its high intensity suggests low crystallinity [70]. The 1480 cm^{-1} (*F*) band, known for fullerenes and fullerites, indicates the atomic structure peculiarities and has been observed in glassy carbon [71]. Upon pyrolysis of IP-L, a commercial acrylate-based TPL photoresist, glassy carbon formation was reported [42]. These IP-L organic constituents are similar to the custom-made photoresist applied in our study [42]. We hypothesize that a similar carbon-based side-product can form within the core of the micropillars.
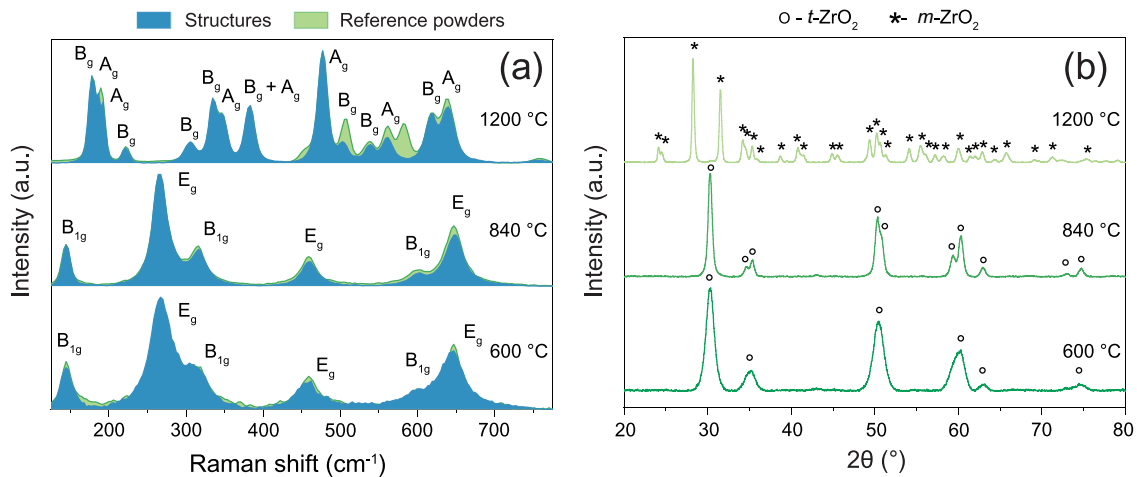
Fig. 2. (a) Confocal Raman spectra collected from the micropillars and reference powders annealed at 600 °C, 840 °C, and 1200 °C for one hour in the 125 – 775 cm^{-1} range; t-ZrO$_2$ (B$_{1g}$ and E$_g$) and m-ZrO$_2$ (A$_g$ and B$_g$) modes are indicated; (b) X-ray powder diffraction patterns of the control samples thermally treated at 600 °C, 840 °C, and 1200 °C for 1 h; t-ZrO$_2$ is labeled with circles (○) and m-ZrO$_2$ with asterisks (*).

Due to the relatively thick cross-section of several μm, the complete combustion of the carbon-rich constituents may be hindered, and the ceramic surface layer formed from the metal–organic precursor could act as an additional barrier. The intensity and area of bands associated with carbon are insignificant for the samples annealed at 840 °C and 1200 °C. The Raman analysis confirms that micropillars obtained after the thermal treatment at 600 °C comprise t-ZrO$_2$ nanocrystals with a side-product containing sp^2 carbon of likely disordered graphitic character [37,42]. The treatment at 840 °C results in the t-ZrO$_2$, and at 1200 °C yields m-ZrO$_2$ with limited carbon content in both cases.

To validate the findings of Raman spectroscopy analysis, additional control powders are prepared from bulk UV-cured photoresin thermally processed under the same conditions as the micropillars. The Raman spectra are well-matched between the powders and 3D structures, show no prominent features at the range related to carbon, and are consistent with our previous results (Fig. 2(a)) [33]. For the reference powder annealed at 1200 °C, weak *H* group signals at the 900 – 1050 cm^{-1} range are observed, being the Raman combinations and overtones [68]. Additionally, for cross-confirmation with Raman spectroscopy, the control powders are characterized using X-ray powder diffraction (XRD). The t-ZrO$_2$ and m-ZrO$_2$ peaks are labeled in Fig. 2(b), and their positions are given (Section SI2, Supporting Information). The diffractograms indicate the correct assignment of the sample phase composition with Raman. Diffractograms registered for the control samples thermally treated at 600 °C and 840 °C show typical t-ZrO$_2$ (P4$_2$/nmc space group) reflections [63,72,73]. Some medium and low-intensity signals overlapped for the first sample. For the sample annealed at 1200 °C, a distinctive pattern of m-ZrO$_2$ (P2$_1$/c space group) is registered [63,74]. Peaks specific for graphitic carbon or allotropes are not found [75,76]. The crystallite sizes are estimated using the Scherrer equation (Supporting Information) for t-ZrO$_2$ (101) and m-ZrO$_2$ ($\bar{1}$11) reflections, which are the most intense peaks. The spherical crystallite shape is assumed for simplicity, and values of 7 nm, 14.5 nm, and 27.5 nm are computed for 600 °C, 840 °C, and 1200 °C, respectively. The t-ZrO$_2$ crystallite sizes are in agreement with the approximate values estimated using Raman spectroscopy.

Even though m-ZrO$_2$ generally exhibits higher stability than other phases at room temperature, stable t-ZrO$_2$ has also been observed under these conditions for various synthesis methods [45,77]. Below certain critical particle size (14 nm [78], or 18 nm

[79]) [78], t-ZrO$_2$ phase can be sustained, over which transformation to m-ZrO$_2$ is induced [79]. Several experimental and numerical studies have focused on the particle-size dependency of polymorph stability, which may be influenced by the synthesis route, particle morphology, and used precursors [80]. The exact stabilization-destabilization mechanisms are still debated [80]. We propose that in this study, a combustible organic matrix of a photopolymer may hinder seed growth and crystallite sintering, thereby promoting the t-ZrO$_2$ formation and stabilization at 600 °C and 840 °C.

The control powder samples are additionally analyzed using X-ray photoelectron spectroscopy (XPS). The general survey confirms the presence of Zr, O, and C, with a minor amount of Hf (Fig. S2, Supporting Information). Hf is one of the main impurities often found in Zr (typical Hf levels in Zr are 1–3 wt%) [81,82]. The deconvolved Zr *3d*, C *1 s*, and O *1 s* core spectra (Fig. S3) indicate that for 600 °C and 840 °C, the contribution of stoichiometric ZrO$_2$ is non-dominant, while for 1200 °C it appears to be the main product. The non-stoichiometric zirconium oxide might be explained by the hindered oxidation of the thick preceramic polymer, as observed for thick films by Lackner *et al.* [83] The Zr to C and O ratio (at.%) decreases with the annealing temperature and is 1:5.16:1.73 for 600 °C, 1:5.38:1.81 for 840 °C, and 1:5.78:2.02 for 1200 °C, suggesting the gradual change from oxygen-deficient zirconium oxide towards of stoichiometric ZrO$_2$, consistent with the proposed explanation. Metallic Zr signals are not observed [84,85].

3.2. Mechanical properties of 3D printed ZrO$_2$ structures

In-situ compression testing is used to evaluate the mechanical properties of the 3D-printed ZrO$_2$ structures and the influence of the previously evidenced organic content. First, the compression strength of plain ZrO$_2$ micropillars is evaluated to single out the material contribution to the mechanical properties of additively-manufactured ZrO$_2$ 3D items. Finally, the structural influence is showcased for two different microarchitectures (Kelvin cell and rhombicuboctahedron-inspired cell).

3.2.1. Intrinsic strength

Compression tests are conducted using plain micropillars to exclude the structural effects inherent to the mechanical properties of 3D additively-manufactured ZrO$_2$ structures (Fig. 3). This way, predominantly material-related characteristics are investi-
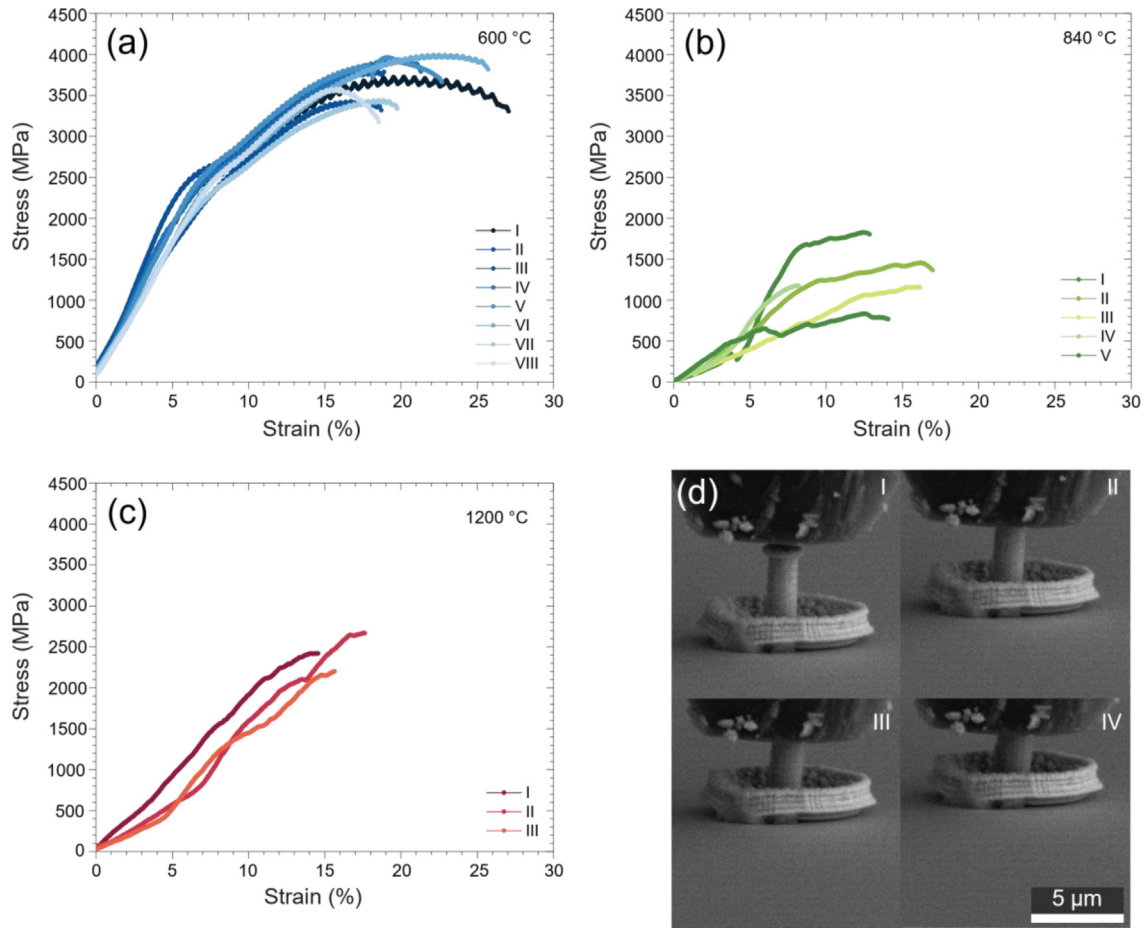
Fig. 3. (a – c) Stress–strain compression curves for micropillars annealed at (a) 600 °C, (b) 840 °C, and (c) 1200 °C; (d) SEM images at different stages (I – IV) of compression for micropillar annealed at 600 °C.

gated. The micropillars are compressed until their fracture occurs; see Fig. 3(d). A representative video of the micropillar compression test is provided in the Supporting Information (Video 1). Care is taken to exclude pillars that are non-vertical following anisotropic shrinkage during sintering. Some pillar compression tests show a non-linear transient at the beginning of loading, which can be attributed to non-ideal contact between the flat punch tip and the upper pillar side. This could be due to surface roughness or a small initial misalignment to the punch surface. The follow-up linear segment is back-extrapolated to zero stress to correct for this initial transient, and the strain data shifted accordingly.

The specimens heat treated at 1200 °C and 840 °C evidence brittle-like failure, respectively, at 2.43 ± 0.19 GPa and 1.29 ± 0.33 GPa. In contrast, the micropillars annealed at 600 °C exhibit strikingly higher ductility and strength (3.73 ± 0.21 GPa). A first explanation for this trend could be a difference in porosity of the pillars [86], all the more so as a difference in density is also suggested by the different stiffnesses measured from the initial linear segment of the stress–strain diagrams (18.1 ± 1.1 GPa, 9.7 ± 2.2 GPa, and 36.4 ± 3.6 GPa for the pillars annealed at 1200 °C, 840 °C, and 600 °C, respectively, see Fig. 3). Indeed, focused ion beam (FIB) milled cross-sections exhibit a consistent increase in porosity with the heat treatments (Fig. 4). While a dense morphology is found for the micropillars annealed at 600 °C (Fig. 4(a)), which also exhibit the highest stiffness, annealing from 840 °C onwards yields micropillars with increased porosity (Fig. 4(b)). It is expected that this high porosity causes the significantly higher scattering of the data in Fig. 3(b) because the pores can act as a fracture initiation

sites. Finally, heat treatment at 1200 °C leads to grain coarsening, with fewer but much larger pores confined to the grain boundaries (Fig. 4(c)).

The aforementioned difference in ductility and strength cannot be solely ascribed to the porosity; otherwise, the sample with the largest pores (1200 °C) would be the most brittle. It is also not solely connected to the crystallographic phase induced by the heat treatment – even though the literature points to a higher ductility of t-ZrO$_2$ [87]. Both samples annealed at 600 °C and 840 °C are composed of t-ZrO$_2$, while m-ZrO$_2$ is present after heat treatment at 1200 °C. The likeliest explanation for the unexpectedly superior mechanical behavior of the specimens annealed at 600 °C is its dual organic-ceramic character, reminiscent of "brick and mortar" composites well-known for their excellent trade-off between strength and ductility. This is, e.g., the case of remarkable biomaterials, such as the nacre of abalone shells [88].

Comparison to reference ceramic materials finds the measured strength is in the upper range of bulk zirconia and yttria-stabilized zirconia (1.2 GPa to 5.2 GPa), while the ductility is much higher [89,90].

3.2.2. Structural effects

We fabricated Kelvin and rhombicuboctahedron-inspired cells (Figs. 5 and 6) to showcase the structural effects introduced by AM. This section focuses on the samples annealed at both extrema of 600 °C and 1200 °C. Selected videos collected by SEM during the compression experiments on the representative structures are provided in Supporting Videos 2 and 3 (Supporting Information).
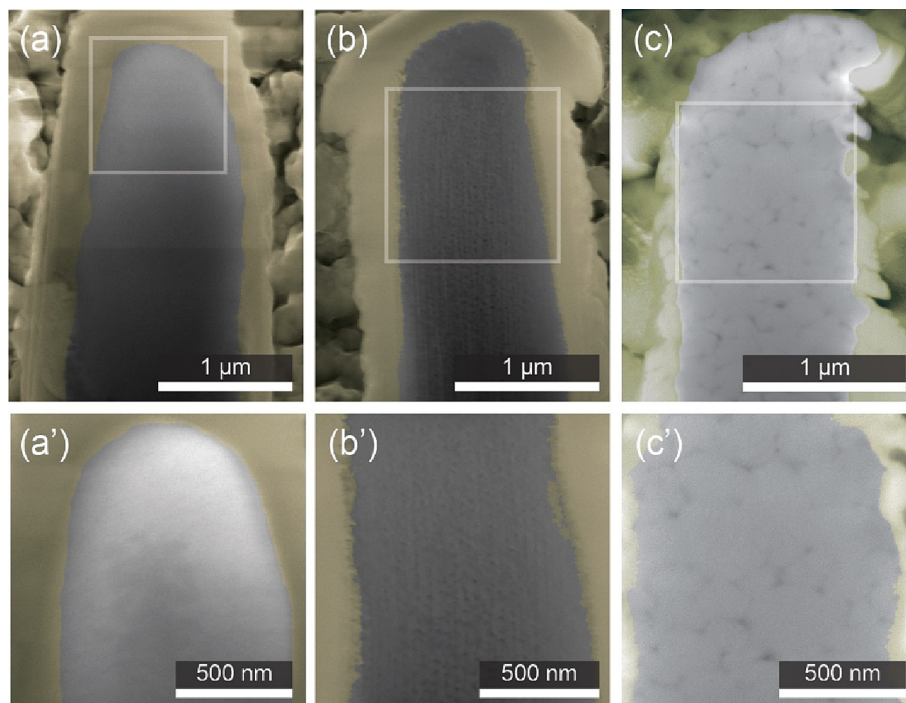
Fig. 4. FIB-milled cross-sections of pristine micropillars after annealing at (a) 600 °C for 1 h, (b) 840 °C for 1 h, and (c) 1200 °C for 1 h. In (a' – c'), higher magnifications of regions labeled with boxes in (a – c), showing the pillar porosity, are presented. The micrographs display secondary electron contrast; the yellow shaded area corresponds to a protection Pt layer added for imaging purposes, which is not part of the ZrO_2 micropillars. (For interpretation of the references to colour in this figure legend, the reader is referred to the web version of this article.)
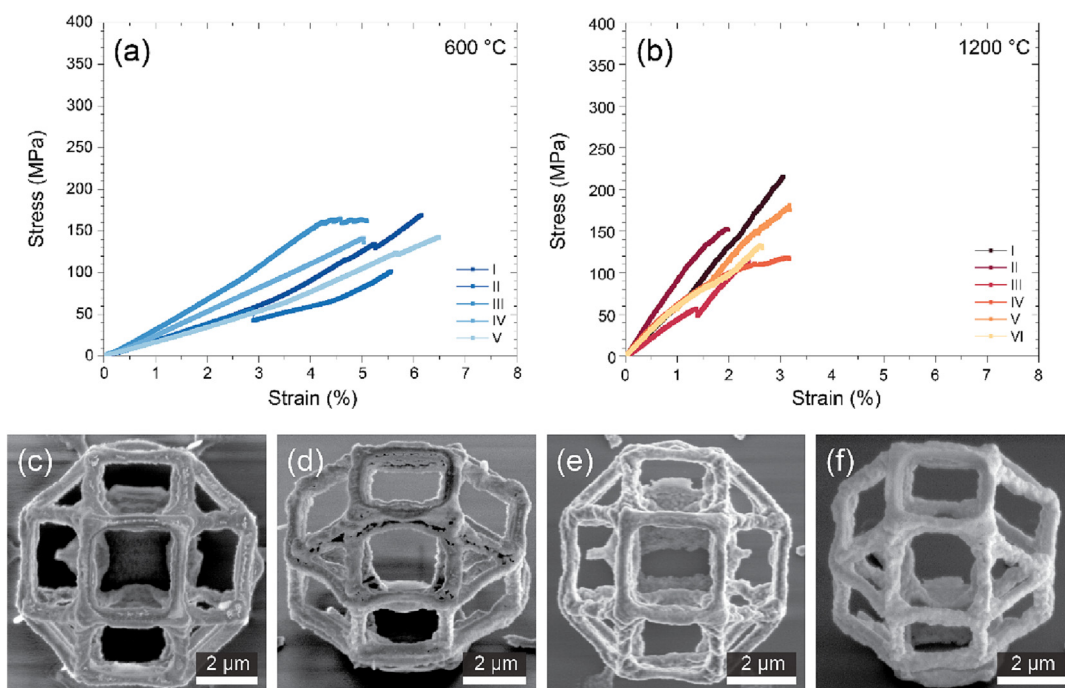

Fig. 5. Stress *vs.* strain curves collected for the rhombicuboctahedron-inspired cells annealed at (a) 600 °C and (b) 1200 °C; top-view and 45° tilt SEM images of rhombicuboctahedron-inspired cells annealed at (c – d) 600 °C and (e – f) 1200 °C.

In comparison to the uniaxial compression of the micropillars, the measured stress–strain diagrams evidence a much smaller strain at failure. The Kelvin and rhombicuboctahedron-inspired cells failed due to locally-induced bending and tensile stresses in the single beams. In this regard, the rhombicuboctahedron-inspired cells perform more poorly than the Kelvin cells due to their longer beams and higher bending stresses. This could also be a reason for the higher scattering observed in Fig. 3 because the structures are more prone to irregularities attributed to the printing and annealing process. Furthermore, the pores randomly
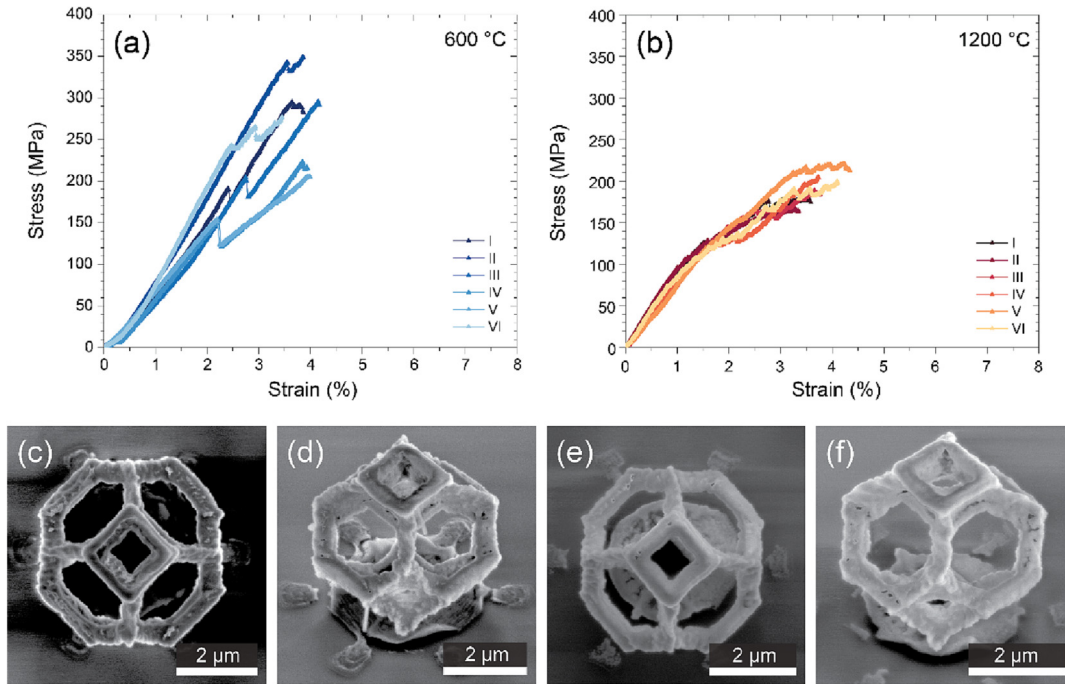
Fig. 6. Stress *vs.* strain curves collected for the Kelvin cells annealed at (a) 600 °C and (b) 1200 °C; top-view and 45° tilt SEM images of Kelvin cells annealed at (c – d) 600 °C and (e – f) 1200 °C.
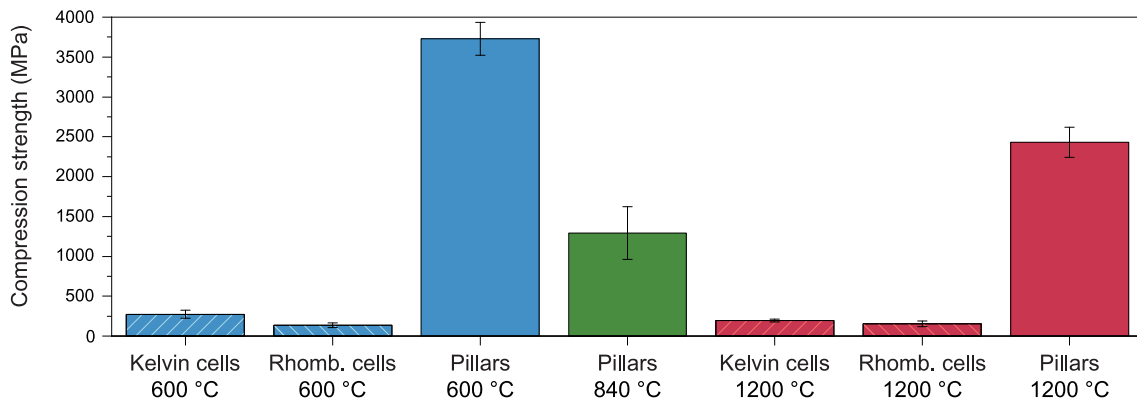

Fig. 7. Compression strength comparison for the pillars, Kelvin cells, and rhombicuboctahedron-inspired cells (Rhomb. cell) annealed at 600 °C, 840 °C, and 1200 °C.

distributed along the grain boundaries in the 1200 °C samples (Fig. 4(c)) can also act as fracture initiation sites and enhance the scattering. The brittleness of the microarchitectures limits the positive effects of the brick-and-mortar composite found in the specimens annealed at 600 °C.

This is obvious from Fig. 7, which compares the measured strength of pillars, Kelvin cells, and rhombicuboctahedron-inspired cells at 600 °C, 840 °C, and 1200 °C.

The structural effect of AM results in a decrease in strength by one order of magnitude. The complex geometry induces combined bending, compressive, and tensile stresses, decreasing overall performance. Desponds *et al.* measured compression strengths below 10 MPa for ZrO$_2$ microarchitectures (tetradecahedrons), but there is some uncertainty about the reference area used for their stress calculation [25]. Other authors use the footprint area, which could be seen as a "global stress" approach [16]. In the current work, we used a "localized stress" approach (see SI 6 in the Supporting Information) to compare the results with those from the pillar compressions. Different areas render it difficult to compare results from

different authors, which should further underline the importance of a uniform testing methodology utilizing standardized microstructures, i.e., micropillars.

4. Conclusions

ZrO$_2$ microarchitectures were fabricated using two-photon lithography and tailor-made photoresin. The printed preceramic complex architectures were annealed at 600 °C, 840 °C, and 1200 °C, which allowed tuning of the crystallographic phase of ZrO$_2$, and the content of carbon-based residues. At 840 °C, and 1200 °C, pure *t*-ZrO$_2$, and *m*-ZrO$_2$ products were obtained. The thermal treatment at 600 °C incorporated significant carbon-based residues in the *t*-ZrO$_2$ product.

The influence of the ZrO$_2$ phase and the carbon-based residues on the mechanical strength of 3D microarchitectures was studied by compression tests. Micropillars were utilized to determine the pure material properties. The mechanical properties of micropillars annealed at 840 °C (*t*-ZrO$_2$) were inferior compared to the samples

treated at 600 °C (t-ZrO_2 with carbon residues) and 1200 °C (m-ZrO_2). The highest strength and ductility of micropillars annealed at 600 °C is attributed to a "brick and mortar" composite formed between nanometric t-ZrO_2 grains and residual carbon. The nature of the carbon can be considered as a mixture of defective or disordered carbon lattice, graphitic carbon species, and amorphous phase. In addition, atomic structure peculiarities similar to glassy-carbon were observed. The increase in the annealing temperature results in the removal of carbon species and promotes the growth of t-ZrO_2, increasing porosity. It can be concluded that the presence of carbon is beneficial for the higher mechanical strength of ceramics obtained within the printed architectures from the photoresin.

For the first time, the role of carbon in polymer-derived ceramic microarchitectures fabricated via two-photon lithography and its influence on mechanical properties is considered. With the presented findings, we underline further importance and opportunities to evaluate the carbon content in ceramic microarchitectures within the TPL community.

CRediT authorship contribution statement

J.P. Winczewski: Conceptualization, Methodology, Validation, Formal analysis, Investigation, Data curation, Writing – original draft, Writing – review & editing, Visualization, Supervision, Project administration. **S. Zeiler:** Methodology, Validation, Formal analysis, Investigation, Data curation, Writing – original draft, Writing – review & editing, Visualization, Project administration. **S. Gabel:** Methodology, Validation, Formal analysis, Investigation, Data curation, Project administration, Writing – review & editing. **A. Susarrey Arce:** Conceptualization, Methodology, Writing – original draft, Writing – review & editing, Supervision, Project administration. **J.G.E. Gardeniers:** Conceptualization, Validation, Resources, Writing – review & editing, Supervision, Project administration, Funding acquisition. **B. Merle:** Conceptualization, Validation, Resources, Writing – review & editing, Supervision, Project administration, Funding acquisition.

Data availability

Data will be made available on request.

Declaration of Competing Interest

The authors declare the following financial interests/personal relationships which may be considered as potential competing interests: J.P. Winczewski, A. Susarrey-Arce, J.G.E. Gardeniers reports financial support was provided by European Research Council (ERC). S. Zeiler, S. Gabel, B. Merle reports financial support was provided by European Research Council (ERC).

Acknowledgments

Appendix A. Supplementary data

Supplementary data to this article can be found online at https://doi.org/10.1016/j.matdes.2023.112142.

References

[1] Q. Chen, J. Zhao, J. Ren, L. Rong, P. Cao, R.C. Advincula, 3D Printed Multifunctional, Hyperelastic Silicone Rubber Foam, Adv. Funct. Mater. 29 (2019) 1900469, https://doi.org/10.1002/adfm.201900469.

[2] Y. Tian, D. Lu, H. Jiang, X. Lin, Preparation of a novel ferrofluidic photoresist for two-photon photopolymerization technique, J. Magn. Magn. Mater. 324 (2012) 3291–3294, https://doi.org/10.1016/j.jmmm.2012.05.019.

[3] Z. Viskadourakis, M. Sevastaki, G. Kenanakis, 3D structured nanocomposites by FDM process: a novel approach for large-scale photocatalytic applications, Appl. Phys. A. 124 (2018) 585, https://doi.org/10.1007/s00339-018-2014-6.

[4] B. Begines, A. Alcudia, R. Aguilera-Velazquez, G. Martinez, Y. He, G.F. Trindade, R. Wildman, M.-J. Sayagues, A. Jimenez-Ruiz, R. Prado-Gotor, Design of highly stabilized nanocomposite inks based on biodegradable polymer-matrix and gold nanoparticles for Inkjet Printing, Sci. Rep. 9 (2019) 16097, https://doi.org/10.1038/s41598-019-52314-2.

[5] Y. Jin, N. Chen, Y. Li, Q. Wang, The selective laser sintering of a polyamide 11/BaTiO₃/graphene ternary piezoelectric nanocomposite, RSC Adv. 10 (2020) 20405–20413, https://doi.org/10.1039/D0RA01042A.

[6] J.Z. Manapat, Q. Chen, P. Ye, R.C. Advincula, 3D Printing of Polymer Nanocomposites via Stereolithography, Macromol. Mater. Eng. 302 (2017) 1600553, https://doi.org/10.1002/mame.201600553.

[7] Q. Hu, X.-Z. Sun, C.D.J.J. Parmenter, M.W. Fay, E.F. Smith, G.A. Rance, Y. He, F. Zhang, Y. Liu, D. Irvine, C. Tuck, R. Hague, R. Wildman, Additive manufacture of complex 3D Au-containing nanocomposites by simultaneous two-photon polymerisation and photoreduction, Sci. Rep. 7 (2017) 17150, https://doi.org/10.1038/s41598-017-17391-1.

[8] C.N. LaFratta, J.T. Fourkas, T. Baldacchini, R.A. Farrer, Multiphoton Fabrication, Angew. Chemie Int. Ed. 46 (2007) 6238–6258, https://doi.org/10.1002/anie.200603995.

[9] T. Baldacchini, J.T. Fourkas, Three-Dimensional Microfabrication Using Two-photon Polymerization, 2nd ed., Elsevier, Oxford, United Kingdom, 2016, https://doi.org/10.1016/C2014-0-01016-7.

[10] B.H. Cumpston, S.P. Ananthavel, S. Barlow, D.L. Dyer, J.E. Ehrlich, L.L. Erskine, A. A. Heikal, S.M. Kuebler, I.-Y.-S. Lee, D. McCord-Maughon, J. Qin, H. Röckel, M. Rumi, X.-L. Wu, S.R. Marder, J.W. Perry, Two-photon polymerization initiators for three-dimensional optical data storage and microfabrication, Nature 398 (1999) 51–54, https://doi.org/10.1038/17989.

[11] U. Staudinger, G. Zyla, B. Krause, A. Janke, D. Fischer, C. Esen, B. Voit, A. Ostendorf, Development of electrically conductive microstructures based on polymer/CNT nanocomposites via two-photon polymerization, Microelectron. Eng. 179 (2017) 48–55, https://doi.org/10.1016/j.mee.2017.04.024.

[12] R. Nakamura, K. Kinashi, W. Sakai, N. Tsutsumi, Fabrication of gold microstructures using negative photoresists doped with gold ions through two-photon excitation, Phys. Chem. Chem. Phys. 18 (2016) 17024–17028, https://doi.org/10.1039/C6CP02577C.

[13] A. Marino, J. Barsotti, G. de Vito, C. Filippeschi, B. Mazzolai, V. Piazza, M. Labardi, V. Mattoli, G. Ciofani, Two-Photon Lithography of 3D Nanocomposite Piezoelectric Scaffolds for Cell Stimulation, ACS Appl. Mater. Interfaces. 7 (2015) 25574–25579, https://doi.org/10.1021/acsami.5b08764.

[14] M. Suter, L. Zhang, E.C. Siringil, C. Peters, T. Luehmann, O. Ergeneman, K.E. Peyer, B.J. Nelson, C. Hierold, Superparamagnetic microrobots: fabrication by two-photon polymerization and biocompatibility, Biomed. Microdev. 15 (2013) 997–1003, https://doi.org/10.1007/s10544-013-9791-7.

[15] W. Xiong, Y. Liu, L.J. Jiang, Y.S. Zhou, D.W. Li, L. Jiang, J. Silvain, Y.F. Lu, Laser-Directed Assembly of Aligned Carbon Nanotubes in Three Dimensions for Multifunctional Device Fabrication, Adv. Mater. 28 (2016) 2002–2009, https://doi.org/10.1002/adma.201505516.

[16] A. Vyatskikh, S. Delalande, A. Kudo, X. Zhang, C.M. Portela, J.R. Greer, Additive manufacturing of 3D nano-architected metals, Nat. Commun. 9 (2018) 593, https://doi.org/10.1038/s41467-018-03071-9.

[17] D.W. Yee, M.L. Lifson, B.W. Edwards, J.R. Greer, Additive Manufacturing of 3D-Architected Multifunctional Metal Oxides, Adv. Mater. 31 (2019) 1901345, https://doi.org/10.1002/adma.201901345.

[18] J.S. Oakdale, J. Ye, W.L. Smith, J. Biener, Post-print UV curing method for improving the mechanical properties of prototypes derived from two-photon lithography, Opt. Express. 24 (2016) 27077, https://doi.org/10.1364/OE.24.027077.

[19] J. Bauer, A. Guell Izard, Y. Zhang, T. Baldacchini, L. Valdevit, Programmable Mechanical Properties of Two-Photon Polymerized Materials: From Nanowires to Bulk, Adv. Mater. Technol. 4 (2019) 1900146, https://doi.org/10.1002/admt.201900146.

[20] J. Bauer, A. Schroer, R. Schwaiger, O. Kraft, The Impact of Size and Loading Direction on the Strength of Architected Lattice Materials, Adv. Eng. Mater. 18 (2016) 1537–1543, https://doi.org/10.1002/adem.201600235.

[21] C.M. Kurpiers, S. Hengsbach, R. Schwaiger, Architectural tunability of mechanical metamaterials in the nanometer range, MRS Adv. 6 (2021) 507–512, https://doi.org/10.1557/s43580-021-00094-1.

[22] L. Jiang, W. Xiong, Y. Zhou, Y. Liu, X. Huang, D. Li, T. Baldacchini, L. Jiang, Y. Lu, Performance comparison of acrylic and thiol-acrylic resins in two-photon polymerization, Opt. Express. 24 (2016) 13687, https://doi.org/10.1364/OE.24.013687.

[23] A. Doraiswamy, A. Ovsianikov, S. Gittard, N. Monteiro-Riviere, R. Crombez, E. Montalvo, W. Shen, B. Chichkov, R. Narayan, Fabrication of Microneedles Using Two Photon Polymerization for Transdermal Delivery of Nanomaterials, J. Nanosci. Nanotechnol. 10 (2010) 6305–6312, https://doi.org/10.1166/jnn.2010.2636.

[24] K.-W. Yeung, Y. Dong, L. Chen, C.-Y. Tang, W.-C. Law, G.-C.-P. Tsui, D.S. Engstrøm, Printability of photo-sensitive nanocomposites using two-photon polymerization, Nanotechnol. Rev. 9 (2020) 418–426, https://doi.org/10.1515/ntrev-2020-0031.

[25] A. Desponds, A. Banyasz, D. Chateau, A. Tellal, A. Venier, S. Meille, G. Montagnac, J. Chevalier, C. Andraud, P.L. Baldeck, S. Parola, 3D Printing and Pyrolysis of Optical ZrO₂ Nanostructures by Two-Photon Lithography: Reduced Shrinkage and Crystallization Mediated by Nanoparticles Seeds, Small. 17 (2021) 2102486, https://doi.org/10.1002/smll.202102486.

[26] J. Bauer, A. Schroer, R. Schwaiger, O. Kraft, Approaching theoretical strength in glassy carbon nanolattices, Nat. Mater. 15 (2016) 438–443, https://doi.org/10.1038/nmat4561.

[27] J. Bauer, S. Hengsbach, I. Tesari, R. Schwaiger, O. Kraft, High-strength cellular ceramic composites with 3D microarchitecture, Proc. Natl. Acad. Sci. 111 (2014) 2453–2458, https://doi.org/10.1073/pnas.1315147111.

[28] J. Arriaga Dávila, J.P. Winczewski, M. Herrera-Zaldívar, E.A. Murillo-Bracamontes, C. Rosero Arias, N. Pineda-Aguilar, J.L. Cholula-Díaz, I. De Leon, H. Gardeniers, A. Susarrey Arce, E. Martínez-Guerra, Enabling high-quality transparent conductive oxide on 3D printed ZrO₂ architectures through atomic layer deposition, Appl. Surf. Sci. 636 (2023) 157796, https://doi.org/10.1016/j.apsusc.2023.157796.

[29] L. Brigo, J.E.M. Schmidt, A. Gandin, N. Michieli, P. Colombo, G. Brusatin, 3D Nanofabrication of SiOC Ceramic Structures, Adv. Sci. 5 (2018) 1800937, https://doi.org/10.1002/advs.201800937.

[30] A. Vyatskikh, R.C. Ng, B. Edwards, R.M. Briggs, J.R. Greer, Additive Manufacturing of High-Refractive-Index, Nanoarchitected Titanium Dioxide for 3D Dielectric Photonic Crystals, Nano Lett. 20 (2020) 3513–3520, https://doi.org/10.1021/acs.nanolett.0c00454.

[31] L. Guo, H. Xia, H. Fan, Y.-L. Zhang, Q. Chen, T. Zhang, H.-B. Sun, Femtosecond laser direct patterning of sensing materials toward flexible integration of micronanosensors, Opt. Lett. 35 (2010) 1695, https://doi.org/10.1364/OL.35.001695.

[32] X. Wen, B. Zhang, W. Wang, F. Ye, S. Yue, H. Guo, G. Gao, Y. Zhao, Q. Fang, C. Nguyen, X. Zhang, J. Bao, J.T. Robinson, P.M. Ajayan, J. Lou, 3D-printed silica with nanoscale resolution, Nat. Mater. 20 (2021) 1506–1511, https://doi.org/10.1038/s41563-021-01111-2.

[33] J. Winczewski, M. Herrera, C. Cabriel, I. Izeddin, S. Gabel, B. Merle, A. Susarrey Arce, H. Gardeniers, Additive Manufacturing of 3D Luminescent ZrO₂: Eu³⁺ Architectures, Adv. Opt. Mater. 10 (2022) 2102758, https://doi.org/10.1002/adom.202102758.

[34] J. Konopka, Options for quantitative analysis of light elements by SEM/EDS, Thermo Fish, Sci. Tech. Note 52523 (2013) 1–4. https://assets.thermofisher.com/TFS-Assets/CAD/Warranties/TN52523_E_0713M_LightElement_H.pdf.

[35] Q. Wen, Z. Yu, R. Riedel, The fate and role of in situ formed carbon in polymer-derived ceramics, Prog. Mater. Sci. 109 (2020) 100623, https://doi.org/10.1016/j.pmatsci.2019.100623.

[36] A. Vyatskikh, R.C. Ng, B. Edwards, R. Julia, A. Vyatskikh, R.C. Ng, B. Edwards, J.R. Greer, Dioxide for Dielectric Photonic Crystals, Proc. SPIE 10930 (2019), https://doi.org/10.1117/12.2507076/.

[37] S.-K. Jerng, D. Seong Yu, J. Hong Lee, C. Kim, S. Yoon, S.-H. Chun, Graphitic carbon growth on crystalline and amorphous oxide substrates using molecular beam epitaxy, Nanoscale Res. Lett. 6 (2011) 565, https://doi.org/10.1186/1556-276X-6-565.

[38] M.J. Shea, M.H. Wall, Representative raman measurements of carbon nanotubes, Spectrosc. Eur. 24 (2012). https://www.spectroscopyeurope.com/article/representative-raman-measurements-carbon-nanotubes.

[39] Y. Wang, D.C. Alsmeyer, R.L. McCreery, Raman spectroscopy of carbon materials: structural basis of observed spectra, Chem. Mater. 2 (1990) 557–563, https://doi.org/10.1021/cm00011a018.

[40] M. Malinauskas, S. Sakirzanovas, V. Padolskyte, D. Gailevicius, V. Mizeikis, K. Staliunas, S. Juodkazis, L. Jonusauskas, L. Mikoliunaite, T. Katkus, R. Gadonas, 3D opto-structuring of ceramics at nanoscale, in: G. von Freymann, A.M. Herkommer, M. Flury (Eds.), 3D Print. Opt. Addit. Photonic Manuf., SPIE, 2018: p. 28, https://doi.org/10.1117/12.2306883.

[41] D. Gailevičius, V. Padolskytė, L. Mikoliūnaitė, S. Šakirzanovas, S. Juodkazis, M. Malinauskas, Additive-manufacturing of 3D glass-ceramics down to nanoscale resolution, Nanoscale Horizons 4 (2019) 647–651, https://doi.org/10.1039/C8NH00293B.

[42] A. Zakhurdaeva, P.-I. Dietrich, H. Hölscher, C. Koos, J. Korvink, S. Sharma, Custom-Designed Glassy Carbon Tips for Atomic Force Microscopy, Micromachines 8 (2017) 285, https://doi.org/10.3390/mi8090285.

[43] K. Li, Y. Shen, G. Fei, H. Wang, C. Wang, The effect of PETA/PETTA composite system on the performance of UV curable waterborne polyurethane acrylate, J. Appl. Polym. Sci. 132 (2015) 1–8, https://doi.org/10.1002/app.41262.

[44] V.V. Rodaev, S.S. Razlivalova, A.O. Zhigachev, V.M. Vasyukov, Y.I. Golovin, Preparation of Zirconia Nanofibers by Electrospinning and Calcination with Zirconium Acetylacetonate as Precursor, Polymers (Basel) 11 (2019) 1067, https://doi.org/10.3390/polym11061067.

[45] N.C. Horti, M.D. Kamatagi, S.K. Nataraj, M.N. Wari, S.R. Inamdar, Structural and optical properties of zirconium oxide (ZrO₂) nanoparticles: effect of calcination temperature, Nano Express. 1 (1) (2020) 010022, https://doi:10.1088/2632-959X/ab8684.

[46] C. Gautam, J. Joyner, A. Gautam, J. Rao, R. Vajtai, Zirconia based dental ceramics: structure, mechanical properties, biocompatibility and applications, Dalt. Trans. 45 (2016) 19194–19215, https://doi.org/10.1039/C6DT03484E.

[47] T. Xiao, T. Liu, G. Xu, Y. Zhang, Phase tuning of ZrO₂ supported cobalt catalysts for hydrodeoxygenation of 5-hydroxymethylfurfural to 2,5-dimethylfuran under mild conditions, Appl. Catal. B Environ. 295 (2021) 120270, https://doi.org/10.1016/j.apcatb.2021.120270.

[48] A. Patra, C.S. Friend, R. Kapoor, P.N. Prasad, Upconversion in Er³⁺:ZrO₂ Nanocrystals, J. Phys. Chem. B 106 (2002) 1909–1912, https://doi.org/10.1021/jp013576z.

[49] R.A. Bapat, H.J. Yang, T.V. Chaubal, S. Dharmadhikari, A.M. Abdulla, S. Arora, S. Rawal, P. Kesharwani, Review on synthesis, properties and multifarious therapeutic applications of nanostructured zirconia in dentistry, RSC Adv. 12 (2022) 12773–12793, https://doi.org/10.1039/D2RA00006G.

[50] V.G. Keramidas, W.B. White, Raman Scattering Study of the Crystallization and Phase Transformations of ZrO₂, J. Am. Ceram. Soc. 57 (1974) 22–24, https://doi.org/10.1111/j.1151-2916.1974.tb11355.x.

[51] D.K. Smith, W. Newkirk, The crystal structure of baddeleyite (monoclinic ZrO₂) and its relation to the polymorphism of ZrO₂, Acta Crystallogr. 18 (1965) 983–991, https://doi.org/10.1107/S0365110X65002402.

[52] A. Bumajdad, A.A. Nazeer, F. Al Sagheer, S. Nahar, M.I. Zaki, Controlled Synthesis of ZrO₂ Nanoparticles with Tailored Size, Morphology and Crystal Phases via Organic/Inorganic Hybrid Films, Sci. Rep. 8 (2018) 3695, https://doi.org/10.1038/s41598-018-22088-0.

[53] A. Ovsianikov, J. Viertl, B. Chichkov, M. Oubaha, B. MacCraith, I. Sakellari, A. Giakoumaki, D. Gray, M. Vamvakaki, M. Farsari, C. Fotakis, Ultra-Low Shrinkage Hybrid Photosensitive Material for Two-Photon Polymerization Microfabrication, ACS Nano 2 (2008) 2257–2262, https://doi.org/10.1021/nn800451w.

[54] B. Buchegger, J. Kreutzer, B. Plochberger, R. Wollhofen, D. Sivun, J. Jacak, G.J. Schütz, U. Schubert, T.A. Klar, Stimulated Emission Depletion Lithography with Mercapto-Functional Polymers, ACS Nano 10 (2016) 1954–1959, https://doi.org/10.1021/acsnano.5b05863.

[55] J. Winczewski, M. Herrera, H. Gardeniers, A. Susarrey-Arce, White emission in 3D-printed phosphor microstructures, Chem. Commun. 59 (2023) 3095–3098, https://doi.org/10.1039/D2CC06953A.

[56] P. Serles, M. Haché, J. Tam, A. Maguire, T. Li, G. Wang, K. Sebastian, J. Lou, C. Jia, P.M. Ajayan, J. Howe, Y. Zou, T. Filleter, Mechanically robust pyrolyzed carbon produced by two photon polymerization, Carbon N. Y. 201 (2023) 161–169, https://doi.org/10.1016/j.carbon.2022.09.016.

[57] R.C. Garvie, R.H. Hannink, R.T. Pascoe, Ceramic steel?, Nature 258 (1975) 703–704, https://doiorg/10.1038/258703a0.

[58] G.W. Jang, H.S. Kim, H.C. Choe, M.K. Son, Fracture Strength and Mechanism of Dental Ceramic Crown with Zirconia Thickness, Procedia Eng. 10 (2011) 1556–1560, https://doi.org/10.1016/j.proeng.2011.04.260.

[59] J.C. Watts, P.A. Larson, Dimethylacetamide, in: Kirk-Othmer Encyclopedia of Chemical Technology, 2002, https://doi.org/10.1002/0471238961.0409130523012020.a01.pub2.

[60] V.P. Rajamanickam, L. Ferrara, A. Toma, R. Proietti Zaccaria, G. Das, E. Di Fabrizio, C. Liberale, Suitable photo-resists for two-photon polymerization using femtosecond fiber lasers, Microelectron. Eng. 121 (2014) 135–138, https://doi.org/10.1016/j.mee.2014.04.040.

[61] L.C. Hatanaka, Q. Wang, Z. Cheng, M.S. Mannan, Effect of trimethylolpropane triacrylate cross-linkages on the thermal stability and char yield of poly (methyl methacrylate) nanocomposites, Fire Saf. J. 87 (2017) 65–70, https://doi.org/10.1016/j.firesaf.2016.12.004.

[62] T. Laetsch, R. Downs, Software For Identification and Refinement of Cell Parameters From Powder Diffraction Data of Minerals Using the RRUFF Project and American Mineralogist Crystal Structure Databases, in: Abstr. from 19th Gen. Meet. Int. Mineral. Assoc., Kobe, Japan, 2006.

[63] S.N. Basahel, T.T. Ali, M. Mokhtar, K. Narasimharao, Influence of crystal structure of nanosized ZrO₂ on photocatalytic degradation of methyl orange, Nanoscale Res. Lett. 10 (2015) 73, https://doi.org/10.1186/s11671-015-0780-z.

[64] X. Zhao, D. Vanderbilt, Phonons and lattice dielectric properties of zirconia, Phys. Rev. B. 65 (2002) 075105, https://doi.org/10.1103/PhysRevB.65.075105.

[65] C. Carlone, Raman spectrum of zirconia-hafnia mixed crystals, Phys. Rev. B. 45 (1992) 2079–2084, https://doi.org/10.1103/PhysRevB.45.2079.

[66] E. Djurado, P. Bouvier, G. Lucazeau, Crystallite Size Effect on the Tetragonal-Monoclinic Transition of Undoped Nanocrystalline Zirconia Studied by XRD and Raman Spectrometry, J. Solid State Chem. 149 (2000) 399–407, https://doi.org/10.1006/jssc.1999.8565.

[67] G. Pezzotti, A.A. Porporati, Raman spectroscopic analysis of phase-transformation and stress patterns in zirconia hip joints, J. Biomed. Opt. 9 (2004) 372, https://doi.org/10.1117/1.1647547.

[68] G.G. Siu, M.J. Stokes, Y. Liu, Variation of fundamental and higher-order Raman spectra of ZrO_2 nanograins with annealing temperature, Phys. Rev. B. 59 (1999) 3173–3179, https://doi.org/10.1103/PhysRevB.59.3173.

[69] A. Cuesta, P. Dhamelincourt, J. Laureyns, A. Martínez-Alonso, J.M.D. Tascón, Raman microprobe studies on carbon materials, Carbon N. Y. 32 (1994) 1523–1532, https://doi.org/10.1016/0008-6223(94)90148-1.

[70] A.Y. Lee, K. Yang, N.D. Anh, C. Park, S.M. Lee, T.G. Lee, M.S. Jeong, Raman study of D* band in graphene oxide and its correlation with reduction, Appl. Surf. Sci. 536 (2021) 147990, https://doi.org/10.1016/j.apsusc.2020.147990.

[71] N.A. Solopova, N. Dubrovinskaia, L. Dubrovinsky, Raman spectroscopy of glassy carbon up to 60 GPa, Appl. Phys. Lett. 102 (2013) 121909, https://doi.org/10.1063/1.4798660.

[72] V. Polliotto, E. Albanese, S. Livraghi, S. Agnoli, G. Pacchioni, E. Giamello, Structural, electronic and photochemical properties of cerium-doped zirconium titanate, Catal. Today 340 (2020) 49–57, https://doi.org/10.1016/j.cattod.2018.09.026.

[73] J. Málek, L. Beneš, T. Mitsuhashi, Powder diffraction data and Rietveld refinement of metastable t-ZrO_2 at low temperature, Powder Diffr. 12 (1997) 96–98, https://doi.org/10.1017/S0885715600009519.

[74] C.J. Howard, R.J. Hill, B.E. Reichert, Structures of ZrO_2 polymorphs at room temperature by high-resolution neutron powder diffraction, Acta Crystallogr. Sect. B Struct. Sci. 44 (1988) 116–120, https://doi.org/10.1107/S0108768187010279.

[75] Y. Xu, Y. Lu, X. Zhu, M. Wang, TE-C36 carbon: a new semiconducting phase with an all-sp^3 bonding network, RSC Adv. 8 (2018) 1846–1851, https://doi.org/10.1039/C7RA11448F.

[76] Z.Q. Li, C.J. Lu, Z.P. Xia, Y. Zhou, Z. Luo, X-ray diffraction patterns of graphite and turbostratic carbon, Carbon N. Y. 45 (2007) 1686–1695, https://doi.org/10.1016/j.carbon.2007.03.038.

[77] J.M. Carvalho, L.C.V. Rodrigues, M.C.F.C. Felinto, L.A.O. Nunes, J. Hölsä, H.F. Brito, Structure–property relationship of luminescent zirconia nanomaterials obtained by sol–gel method, J. Mater. Sci. 50 (2015) 873–881, https://doi.org/10.1007/s10853-014-8648-7.

[78] Y.L. Zhang, X.J. Jin, Y.H. Rong, T.Y. Hsu (Xu Zuyao), D.Y. Jiang, J.L. Shi, The size dependence of structural stability in nano-sized ZrO2 particles, Mater. Sci. Eng. A 438-440 (2006) 399–402, doi.org/10.1016/j.msea.2006.03.109.

[79] T. Chraska, A.H. King, C.C. Berndt, On the size-dependent phase transformation in nanoparticulate zirconia, Mater. Sci. Eng. A 286 (2000) 169–178, https://doi.org/10.1016/S0921-5093(00)00625-0.

[80] J.C. Valmalette, M. Isa, Size Effects on the Stabilization of Ultrafine Zirconia Nanoparticles, Chem. Mater. 14 (2002) 5098–5102, https://doi.org/10.1021/cm021233n.

[81] L. Xu, Y. Xiao, A. van Sandwijk, Q. Xu, Y. Yang, Separation of Zirconium and Hafnium: A Review, in: Energy Mater. 2014, John Wiley & Sons, Inc., Hoboken, NJ, USA, 2015: pp. 451–457, https://doi.org/10.1002/9781119027973.ch53.

[82] A.M. Huerta-Flores, F. Ruiz-Zepeda, C. Eyovge, J.P. Winczewski, M. Vandichel, M. Gaberšček, N.D. Boscher, H.J.G.E. Gardeniers, L.M. Torres-Martínez, A. Susarrey-Arce, Enhanced Photocatalytic Hydrogen Evolution from Water Splitting on Ta_2O_5 /$SrZrO_3$ Heterostructures Decorated with Cu_xO/RuO_2 Cocatalysts, ACS Appl. Mater. Interfaces 14 (2022) 31767–31781, https://doi.org/10.1021/acsami.2c02520.

[83] P. Lackner, Z. Zou, S. Mayr, U. Diebold, M. Schmid, Using photoelectron spectroscopy to observe oxygen spillover to zirconia, Phys. Chem. Chem. Phys. 21 (2019) 17613–17620, https://doi.org/10.1039/C9CP03322J.

[84] S.K. Sharma, T. Strunskus, H. Ladebusch, V. Zaporojtchenko, F. Faupel, XPS study of the initial oxidation of the bulk metallic glass $Zr_{46.75}Ti_{8.25}Cu_{7.5}Ni_{10}Be_{27.5}$, J. Mater. Sci. 43 (2008) 5495–5503, https://doi.org/10.1007/s10853-008-2834-4.

[85] I. Takano, S. Isobe, T.A. Sasaki, Y. Baba, Nitrogenation of various transition metals by N^{+2}-ion implantation, Appl. Surf. Sci. 37 (1989) 25–32, https://doi.org/10.1016/0169-4332(89)90970-7.

[86] J. Eichler, U. Eisele, J. Rödel, Mechanical Properties of Monoclinic Zirconia, J. Am. Ceram. Soc. 87 (2004) 1401–1403, https://doi.org/10.1111/j.1151-2916.2004.tb07748.x.

[87] Y. Zhang, H.-X. Chen, J.-B. Duan, L.-J. Fan, L. Ni, V. Ji, A comparison study of the structural and mechanical properties of cubic, tetragonal, monoclinic, and three orthorhombic phases of ZrO_2, J. Alloys Compd. 749 (2018) 283–292, https://doi.org/10.1016/j.jallcom.2018.03.253.

[88] X. Zhang, K. Zhang, L. Zhang, W. Wang, Y. Li, R. He, Additive manufacturing of cellular ceramic structures: From structure to structure–function integration, Mater. Des. 215 (2022) 110470, https://doi.org/10.1016/j.matdes.2022.110470.

[89] AZO Materials, Zirconia - ZrO_2, Zirconium Dioxide, https://www.azom.com/properties.aspx?ArticleID=133 (accessed March 31, 2023).

[90] C. Piconi, G. Maccauro, Zirconia as a ceramic biomaterial, Biomaterials 20 (1999) 1–25, https://doi.org/10.1016/S0142-9612(98)00010-6.